

Nonlinear and detuning effects of the nutation angle in precessionally-forced rotating cylinder flow

Juan M. Lopez

*School of Mathematical and Statistical Sci.,
Arizona State University, Tempe AZ, 85287, USA*

Francisco Marques

Departament de Física Aplicada, Univ. Politècnica de Catalunya, Barcelona 08034, Spain

(Dated: July 18, 2016)

Abstract

The flow in a rapidly rotating cylinder forced to precess through a nutation angle α is investigated numerically, keeping all parameters constants except α , and tuned to a triadic resonance at $\alpha = 1^\circ$. When increasing α , the flow undergoes a sequence of well-characterized bifurcations associated with triadic resonance, involving heteroclinic and homoclinic cycles, for α up to about 4° . For larger α , we identify two chaotic regimes. In the first regime, with α between about 4° and 27° , the bulk flow retains remnants of the helical structures associated with the triadic resonance, but there are strong nonlinear interactions between the various azimuthal Fourier components of the flow. For the larger α regime, large detuning effects lead to the triadic resonance dynamics being completely swamped by boundary layer eruptions. The azimuthal mean flow at large angles results in a large mean deviation from solid-body rotation and the flow is characterized by strong shear at the boundary layers with temporally chaotic eruptions.

I. INTRODUCTION

Precessing flows consist of a fluid-filled body rotating about an axis with rotation vector $\boldsymbol{\omega}_0$ that is itself rotating (precessing) about another rotation vector $\boldsymbol{\omega}_p$, where the angle between the two rotation vectors is α . Examples of precessionally forced flows are plentiful in astrophysics and geophysics [1, 2], as well as in spinning space-crafts with liquid fuels [3, 4]. Furthermore, Earth-based rotating flow experiments can be impacted by precessional forcing if their length scale is sufficiently large and their rotation axis is not aligned with the Earth's rotation axis [5]. Since weak precessional forcing can sustain “turbulence” (or at least spatio-temporally complex flows with desirable mixing properties), precession opens up a number of possible applications in chemical engineering [6, 7].

Weakly precessing flows tend to be dominated by triadic resonances; these have been observed experimentally [8–11], analyzed theoretically [12–14], and simulated numerically [15, 16]. For the most part, these investigations in cylindrical geometries have used small nutation angles α in order to be in the weak precessional forcing regime. Alternatively, $\alpha = 90^\circ$ with very small precession rates also leads to the weak precession regime where triadic resonances have also been observed experimentally [17]. However, those experiments with $\alpha = 90^\circ$ did not detect triadic resonances when the precession rate was too fast. Experimentally, as α is increased above about 4° , the system is observed to suffer a catastrophic transition to small scale apparently disorganized flow, usually reported as being turbulent [8–11]. This regime, and the transition to it, has not been accessible using existing theories, and flow visualization experiments have been inadequate for examining the flow dynamics. More quantitative experimental measurements suffer from not being able to resolve the disparate spatial and temporal scales that are dynamically important. Despite over a century of study, the saturation amplitude of instabilities, the conditions for the apparition of intermittent cycles, the type of turbulence and its associated spectra, and the clarification of the bifurcation sequences leading to turbulence are all still open questions [2, 18]. However, with recent advances in numerical simulations of the full governing equations, insight into some of these intriguing problems has become accessible.

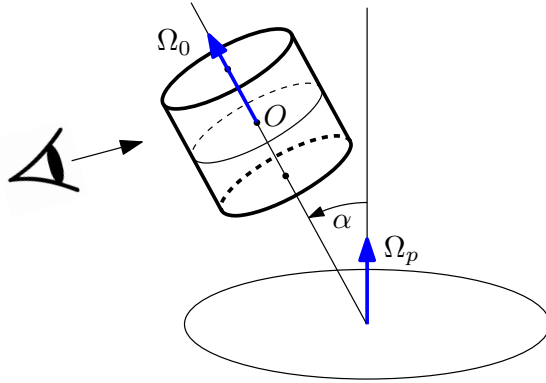


FIG. 1: Schematic of the precessing cylinder, with the axis fixed in a table rotating with angular speed Ω_p . The cylinder rotates about its axis relative to the table with angular speed Ω_0 . The eye of an observer standing on the rotating table indicates the perspective view used for rendering 3D plots of the flow, with the two rotation vectors in the line of view.

II. GOVERNING EQUATIONS AND NUMERICAL TECHNIQUE

The problem under consideration consists of a cylinder of height H and radius R filled with an incompressible fluid of kinematic viscosity ν and rotating about its axis with angular velocity Ω_0 . The cylinder is mounted at the center of a horizontal table that rotates with angular velocity Ω_p around the vertical axis, as shown in Fig. 1. The cylinder axis is tilted an angle α relative to the vertical, and is at rest relative to the table, therefore the cylinder axis precesses with angular velocity Ω_p with respect to the laboratory inertial reference frame. All variables are non-dimensionalized using the cylinder radius R as the length scale and the viscous time R^2/ν as the time scale, as in [16]. The non-dimensional governing parameters are:

$$\text{cylinder rotation} \quad \omega_0 = \Omega_0 R^2 / \nu, \quad (1)$$

$$\text{precession rate} \quad \omega_p = \Omega_p R^2 / \nu, \quad (2)$$

$$\text{aspect ratio} \quad \Gamma = H/R, \quad (3)$$

$$\text{nutations angle} \quad \alpha. \quad (4)$$

It is convenient to also introduce the Poincaré number, $Po = \omega_p/\omega_0$, which provides a viscosity-independent measure of the precessional forcing.

The governing equations are written using cylindrical coordinates (r, θ, z) , fixed in the (rotating) table frame of reference, with the z direction aligned with the cylinder axis, and

the origin O at the center of the cylinder:

$$\partial_t \mathbf{v} + (\mathbf{v} \cdot \nabla) \mathbf{v} = -\nabla p - 2\boldsymbol{\omega}_p \times \mathbf{v} + \Delta \mathbf{v}, \quad \nabla \cdot \mathbf{v} = 0. \quad (5)$$

Note that the theoretical study of inertial waves is usually conducted in a frame of reference that is rotating with the background rotation. In the case of a precessing cylinder flow, this frame is the one in which the cylinder is stationary, i.e. the cylinder frame of reference. This introduces a three-dimensional time-periodic body force, whereas in the table frame of reference the body force is steady (but also three-dimensional) [16]. In the cylinder frame the velocity boundary conditions are zero, whereas in the table frame ω_0 appears in the boundary conditions for the velocity, which correspond to solid-body rotation: $\mathbf{v}|_{\partial\mathcal{D}} = (0, r\omega_0, 0)$. The solid-body rotation is a large component of the velocity field, which makes it difficult to visualize deviations from it. Therefore, we have used the deviation field \mathbf{u} with respect to the solid-body rotation component in order to visualize and study the properties of the solutions: $\mathbf{v} = \mathbf{v}_{SB} + \mathbf{u}$. In cylindrical coordinates, $\mathbf{v}_{SB} = (0, r\omega_0, 0)$ and the deviation velocity field is $\mathbf{u} = (u, v, w)$.

The L_2 -norms of the azimuthal Fourier components of a given solution are

$$E_m = \frac{1}{2} \int_{z=-\Gamma/2}^{z=\Gamma/2} \int_{r=0}^{r=1} \mathbf{u}_m \cdot \mathbf{u}_m^* r \, dr \, dz, \quad (6)$$

where \mathbf{u}_m is the m th azimuthal Fourier components of the deviation velocity field and \mathbf{u}_m^* is its complex conjugate. The solid-body rotation of the cylinder in the table reference system is given by $\mathbf{u}_{SB} = r\omega_0 \hat{\boldsymbol{\theta}}$ and the corresponding kinetic energy is E_{SB} . It is convenient to introduce the modal kinetic energies of the deviation relative to the solid-body rotation kinetic energy, and as they can be time dependent, its maximum value over an appropriate large time interval is used:

$$e_m = \max_t E_m(t)/E_{SB}, \quad E_{SB} = \frac{1}{8} \Gamma \omega_0^2. \quad (7)$$

These provide a convenient way to characterize the different states obtained. Other useful variables are the vorticity field $\nabla \times \mathbf{u} = (\xi, \eta, \zeta)$, and the helicity $\mathcal{H} = \mathbf{u} \cdot (\nabla \times \mathbf{u})$, both defined in terms of \mathbf{u} , the deviation of the velocity field with respect to solid-body rotation, in the table reference frame.

The governing equations have been solved using a second-order time-splitting method, with space discretized via a Galerkin–Fourier expansion in θ and Chebyshev collocation

in r and z . The spectral solver is based on that described in [19], and we have added in the inertial body force. This code, with slight variations, has already been used in a variety of fluid problems [16, 20–23]. For the solutions presented in this study, we have used $n_r = n_z = 64$ Chebyshev modes in the radial and axial directions and $n_\theta = 130$ azimuthal Fourier modes. The number of Chebyshev spectral modes used provides a good resolution of the boundary layers forming at the cylinder walls; the solutions have at least four orders of magnitude of decay in the modal spectral energies.

The cylindrical container is invariant under the action of rotations R_ϕ about the cylinder axis and the reflection K_z about the cylinder mid-plane $z = 0$. However, the body force is equivariant only under the combined action of R_π and K_z , i.e. the action of the inversion $\mathcal{I} = K_z R_\pi$, which is the only spatial symmetry of the system. As the governing equations (5) do not depend explicitly on time, they are equivariant under time translations T_τ . Therefore, the precessing cylinder system in the rotating table frame of reference is equivariant under the group $\mathbb{Z}_2 \times \mathbb{R}^T$, where \mathcal{I} and T_τ are the corresponding generators. As a result, the base state is steady and invariant under inversion. The action of the inversion symmetry \mathcal{I} on the position vector is $\mathcal{I}\mathbf{r} = -\mathbf{r}$, and on the cylindrical coordinates it is $(r, \theta, z) \mapsto (r, \theta + \pi, -z)$. Its action on the velocity and vorticity components and the helicity is

$$\mathcal{A}(\mathcal{I})(u, v, w)(r, \theta, z, t) = (u, v, -w)(r, \theta + \pi, -z, t), \quad (8a)$$

$$\mathcal{A}(\mathcal{I})(\xi, \eta, \zeta)(r, \theta, z, t) = (-\xi, -\eta, \zeta)(r, \theta + \pi, -z, t), \quad (8b)$$

$$\mathcal{A}(\mathcal{I})\mathcal{H}(r, \theta, z, t) = -\mathcal{H}(r, \theta + \pi, -z, t). \quad (8c)$$

The change of sign in the helicity is due to the fact that the helicity is a pseudo-scalar since it is the dot product of a polar and an axial vector [24].

It is also convenient to introduce a symmetry parameter

$$S = \|\mathbf{u} - \mathcal{A}(\mathcal{I})\mathbf{u}\|_2, \quad (9)$$

where $\|\cdot\|_2$ is a discrete L_2 norm defined in [16]. It is zero for \mathcal{I} -invariant solutions, and positive for non-symmetric solutions. For time-dependent solutions, the symmetry parameter is also time dependent, and we will use its maximum value over an appropriate large time interval, $S_M = \max_t S(t)$, in order to characterize the lack of symmetry of the solutions.

III. BACKGROUND

Many theoretical studies on inertial waves consider a cylinder rotating about its axis with angular velocity $Re \hat{z}$, subjected to infinitesimal perturbations. The linearized inviscid equations in the cylinder reference frame admit wavelike solutions (Kelvin modes) of temporal frequency σ if $\sigma < 2Re$. The group velocity of these waves propagates along a direction that makes an angle β with the cylinder mid-plane, given by the dispersion relation $2 \cos \beta = \sigma/Re$ [25]. The Kelvin modes are characterized by three integers (k, m, n) , where m is the azimuthal wavenumber, and k and n are related to the number of zeros in the radial and axial directions respectively. In the rotating and precessing cylinder considered here, $\sigma_{k,m,n}/\omega_0$ depends on Γ , α and the Poincaré number Po ; the details can be found in [16, 23]. The Kelvin modes do not satisfy the no-slip boundary conditions, zero velocity at the walls, but only the weaker condition of zero normal velocity. The zero viscosity limit is singular, and any physical solution resembling Kelvin modes must include boundary layers in order to adjust the velocity to the physical boundary conditions [16, 26].

The Kelvin modes are damped by viscosity, and their physical realization with finite viscosity requires an external forcing to sustain them. In precessing flows, the forcing is provided by the Coriolis body force. In the rotating and precessing cylinder (Fig. 1), the total angular velocity of the cylinder is given by

$$\boldsymbol{\omega}_C = \boldsymbol{\omega}_p + \boldsymbol{\omega}_0 = \boldsymbol{\omega}_\perp + Re \hat{z}. \quad (10)$$

In the table reference frame this is a constant vector. Its axial component (in the direction of the cylinder axis \hat{z}) is $Re = \omega_0 + \omega_p \cos \alpha$, and provides the solid-body rotation of the cylinder around its axis. The orthogonal component $\boldsymbol{\omega}_\perp$, of modulus $|\omega_p| \sin \alpha$, is constant in the table reference frame, and rotates around the cylinder axis with angular velocity ω_0 in the cylinder reference frame. This orthogonal component provides the forcing that may sustain inertial waves. We define the forcing amplitude as

$$A_f = |\boldsymbol{\omega}_\perp|/\omega_0 = |Po| \sin \alpha. \quad (11)$$

Dividing by ω_0 makes the amplitude independent of viscosity, and it is the appropriate definition in the inviscid limit. Although the amplitude of the forcing is independent of the sign of Po , the resulting flow is not.

The precessional forcing is able to excite inertial waves as long as $\omega_0 \leq 2Re$. The body force $-2\boldsymbol{\omega}_p \times \mathbf{v}$ depends explicitly on the azimuthal coordinate θ , $\boldsymbol{\omega}_p = \omega_p(\sin \alpha \sin \theta \hat{\mathbf{r}} + \sin \alpha \cos \theta \hat{\boldsymbol{\theta}} + \cos \alpha \hat{\mathbf{z}})$, due to the nonzero nutation angle α , and therefore has azimuthal wavenumber $m = 1$. The body force is independent of z . Therefore, it excites the $(k, m, n) = (1, 1, 1)$ mode, and the base flow of the viscous nonlinear system (5) resembles the $(1, 1, 1)$ -Kelvin mode, as long as the forcing frequency ω_0 coincides with $\sigma_{1,1,1}$. This gives a relationship between Γ , α and Po , i.e. for a fixed geometry Γ and α , we must use a specific value of the Poincaré number, Po_{res} , in order to excite the $(1, 1, 1)$ -Kelvin mode. Of course, if one uses a forcing frequency $\sigma_{k,1,n}$, then a $(k, 1, n)$ -Kelvin mode (with k and n not necessarily equal to 1) will be resonantly excited, and this has been demonstrated experimentally [8, 12]. All of this is according to linear inviscid theory. In practice, due to viscous and nonlinear effects, and the presence of boundary layers, there is a range of values of Po for which the base flow of the precessing rotating cylinder resembles the $(1, 1, 1)$ -Kelvin mode. The response function, which is a delta function $\delta(Po - Po_{\text{res}})$ for the linear inviscid problem, becomes a finite resonance peak when viscosity is present. The width of the peak depends on viscosity, i.e. the Reynolds number Re , and the height of the peak depends on the amplitude of the forcing A_f .

It is also possible to find resonances between different Kelvin modes. As shown in [11, 13], triadic resonances between the $(1, 1, 1)$ -Kelvin mode and two additional modes (k_1, m_1, n_1) and (k_2, m_2, n_2) are possible when $|n_2 \pm n_1| = 1$, $|m_2 \pm m_1| = 1$, and $|\sigma_{k_2, m_2, n_2} \pm \sigma_{k_1, m_1, n_1}| = \omega_0$. Therefore, by fine-tuning the aspect ratio Γ and the Poincaré number Po (for a given nutation angle α) it is possible to obtain a variety of triadic resonances. For example, the 1:5:6 resonance between the Kelvin modes $(1, 1, 1)$, $(1, 6, 2)$ and $(1, -5, 1)$, for a nutation angle $\alpha_0 = 1^\circ$, takes place for $\Gamma = 1.62$ and $Po = -0.1525$. There has been extensive theoretical, experimental and numerical work on this particular resonance [11, 13, 15, 16], and we continue exploring it in the present paper. In particular, in [16] the forcing was increased by varying ω_0 and ω_p while keeping α , Γ and Po constant, so that the flow was always very close to the 1:5:6 triadic resonance. A complex transitional process through a variety of increasingly complex flows was obtained.

IV. RESULTS

Since the forcing amplitude is given by $A_f = |Po| \sin \alpha$, one can obtain the same forcing amplitude for different α by adjusting Po . Based on this fact and limited nonlinear viscous numerical simulations, it has been suggested that α does not seem to play an important role in the dynamics of precessing flows [27, 28]. This is in sharp contrast with the experimental observations mentioned above [8–11], and motivates our exploring the flow in a precessing cylinder varying the nutation angle α . As mentioned in the previous section, we shall focus on the 1:5:6 triadic resonance regime, keeping $H/R = 1.62$, $\omega_0 = 4000$ and $Po = -0.1525$ fixed, and consider variations in $\alpha \in (0.1^\circ, 47^\circ)$. In this way, the forcing is increased and the system remains close to the triadic resonance 1:5:6 whilst α is not too large. Such an approach is often used experimentally [8, 10]. The effects of α on the dynamics are ascertained, while still being able to compare with previous studies. For large enough α , there will be detuning effects, and these are also explored. Numerically, we start with a very small $\alpha = 0.1^\circ$ to obtain the base state, starting from solid-body rotation as the initial condition. Then, simulations with small increments in α are conducted with the solution at the smaller α as the initial condition. When a qualitative change in behavior is observed, the same type of parameter continuation to lower values of α is implemented to check for multiplicity of states and hysteresis.

The conditions that must be satisfied in order to have a resonant (1, 1, 1)-Kelvin mode, and to also have the 1:5:6 triadic resonance, are that the ratios

$$\frac{\sigma_{1,1,1}}{\omega_0} = \frac{\sigma_{1,-5,1}}{\omega_0} + \frac{\sigma_{1,6,2}}{\omega_0} = \frac{1 + Po \cos \alpha}{1 + Po \cos \alpha_0} = 1 + \delta \quad (12)$$

be equal to one, i.e. that the detuning parameter $\delta = 0$. Fixing $\Gamma = 1.62$, $\omega_0 = 4000$ and $\omega_p = -610$ (corresponding to $Po = -0.1525$), the exact resonance conditions are obtained only for $\alpha = \alpha_0 = 1^\circ$. Keeping Γ , ω_0 and ω_p fixed and varying α , three different regimes have been identified from the Navier–Stokes simulations, described in the following subsections.

A. Weakly nonlinear resonant regime: $\alpha \lesssim 4^\circ$.

When the nutation angle is small, $\alpha \lesssim 1^\circ$, only the forced (1, 1, 1)-Kelvin mode is sufficiently excited by the Coriolis forcing, and the flow in the table frame of reference corresponds to the steady basic state BS, consisting primarily of flow up one side of the cylinder and

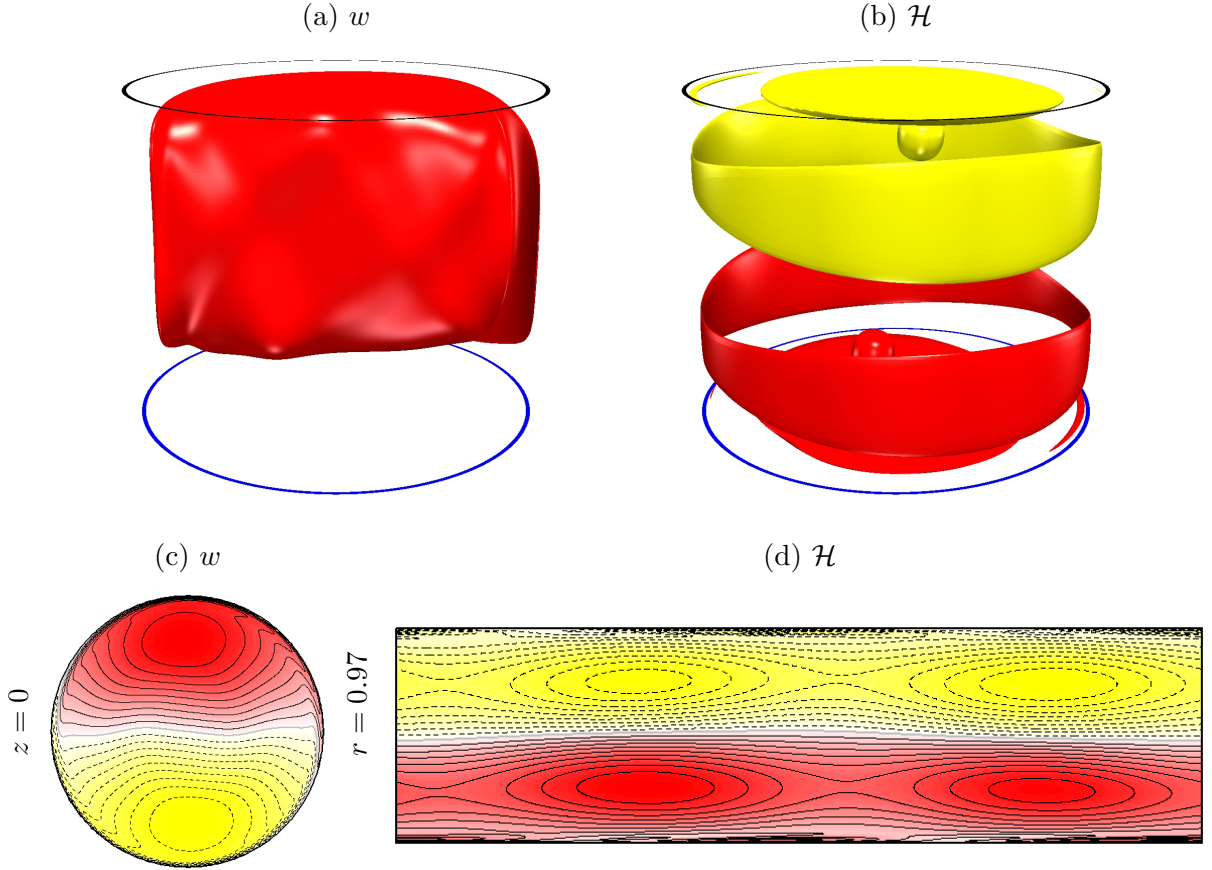


FIG. 2: BS at $\alpha = 1.146^\circ$: isosurfaces of (a) w and (b) \mathcal{H} at levels $w = 40$ & $\mathcal{H} = \pm 1.5 \times 10^5$, and contours of (c) axial velocity at mid-height $z = 0$, and (d) helicity in (θ, z) at $r = 0.97$.

down the other. It is illustrated in the first row of Fig. 2, which shows isosurfaces of the axial velocity, w , and the helicity, \mathcal{H} , at $\alpha = 1.146^\circ$ (0.02 rad). The flow is completely dominated by the overturning flow, as shown by the axial velocity isosurface, and the boundary layers are very smooth and almost axisymmetric, as shown in the helicity isosurfaces. Only the positive w isosurface is shown, corresponding to the upward moving flow. The downward flow is the \mathcal{I} -reflection of the upward flow, as BS is \mathcal{I} -symmetric, located in the other half of the cylinder, and it is not shown for clarity. In the view shown, the axis of the cylinder ω_0 and the axis of the table ω_p are both in the meridional plane orthogonal to the page, as shown schematically in Fig. 1. Figure 2(c) shows contours of axial velocity w in a plane at mid-height, $z = 0$, showing the upward and downward components of the overturning flow. Figure 2(d) shows the helicity of this solution on a cylindrical surface, $\theta \in [0, 2\pi]$ and $z \in [-0.5\Gamma, 0.5\Gamma]$ at $r = 0.97$, essentially at mid-thickness of the sidewall boundary layer. Here, the helicity is positive in the bottom half of the cylinder and negative in the top half,

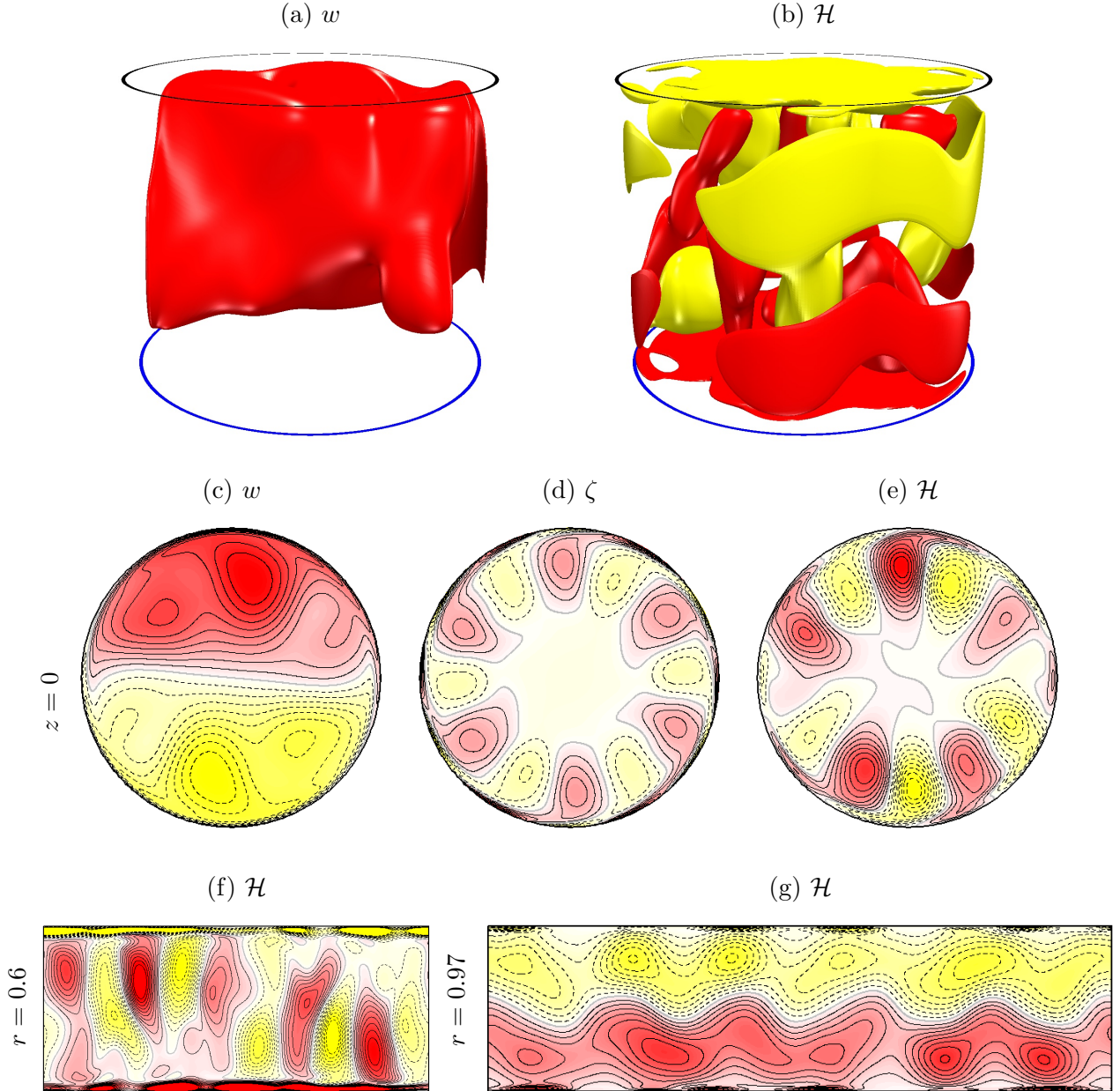


FIG. 3: LC at $\alpha = 1.432^\circ$: isosurfaces of (a) axial velocity and (b) helicity at levels $w = 50$ & $\mathcal{H} = \pm 2 \times 10^5$ (see the online movie [URL will be inserted by publisher]), and contours of (c) axial velocity, (d) axial vorticity, and (e) helicity, at mid-height $z = 0$; there are 20 equispaced contours between the minimum and maximum values in the section. Helicity contours in (θ, z) at (f) $r = 0.6$ and (g) $r = 0.97$; there are 20 contours equispaced between $\mathcal{H} \in [-5 \times 10^5, 5 \times 10^5]$.

and modulated away from being axisymmetric by the $m = 1$ influence of the Coriolis force. The helicity of BS is essentially confined to the boundary layers of the top and bottom endwalls and the sidewall.

The base state BS loses stability when α is increased beyond $\alpha \approx 1.26^\circ$, in a supercritical Hopf bifurcation induced by the 1:5:6 resonance. This results in a limit cycle LC, which is time-periodic in the table frame of reference. This is the same \mathcal{I} -symmetric LC solution branch that is obtained by fixing $\alpha = 1^\circ$, $\Gamma = 1.62$ and $Po = -0.152\,53$, and increasing $\omega_0 \gtrsim 4777$ (see Figs. 3 and 10 in [16]).

The LC solution for $\alpha = 1.432^\circ$ (0.025 rad) is shown in Fig. 3. The first row shows iso-surfaces of the axial velocity and the helicity. Comparing with BS in Fig. 2, the overturning flow in LC has small distortions compared with BS, but the main change is in the helicity. The boundary layers are more complex, and the bulk flow is dominated by helicity columns that are the manifestation of the resonant $m = 5$ and 6 modes. Figure 3(c) shows contours of axial velocity w , and the presence of 5 or 6 perturbations inside the overturning flow are apparent. As was shown in [16], the contours of axial vorticity ζ and helicity \mathcal{H} at mid-height, shown in Fig. 3(d,e), highlight the structure of the $m = 5$ and 6 modes that appear at the Hopf bifurcation. Figure 3(f) shows contours of \mathcal{H} at $r = 0.6$, where the $m = 5$ and 6 modes are most intense. These modes consist of columnar vortices with a well defined helicity, that emerge from the strong top and bottom endwall boundary layers. Figure 3(g) shows contours of \mathcal{H} at $r = 0.97$, essentially in the middle of the sidewall boundary layer. Here, the helicity is positive in the bottom half of the cylinder and negative in the top half, as was the case for BS, but with perturbations induced by the 1:5:6 triadic resonance, with a distinct $m = 5$ oscillation at the mid-plane; see Fig. 3(e). The LC solutions are \mathcal{I} -symmetric, as illustrated in the r -constant contours, and quantified by $S_M = 0$. The online movie corresponding to Fig. 3(b) illustrates the spatio-temporal helical structure of LC.

By increasing the nutation angle up to $\alpha = 4^\circ$, a variety of complex flows are obtained as LC becomes unstable. Figure 4 shows how the energies e_m of the Fourier components of the velocity field vary with α . Note that for BS and LC, the modal energies E_m are time independent (for BS because it is a steady state, and for LC its Fourier components are like rotating waves whose structure are time independent but drift in azimuth, so that their energies are time-independent). However, for the states that result from the instability of LC, their energies are time dependent, and their maxima e_m (defined in (7)) are plotted

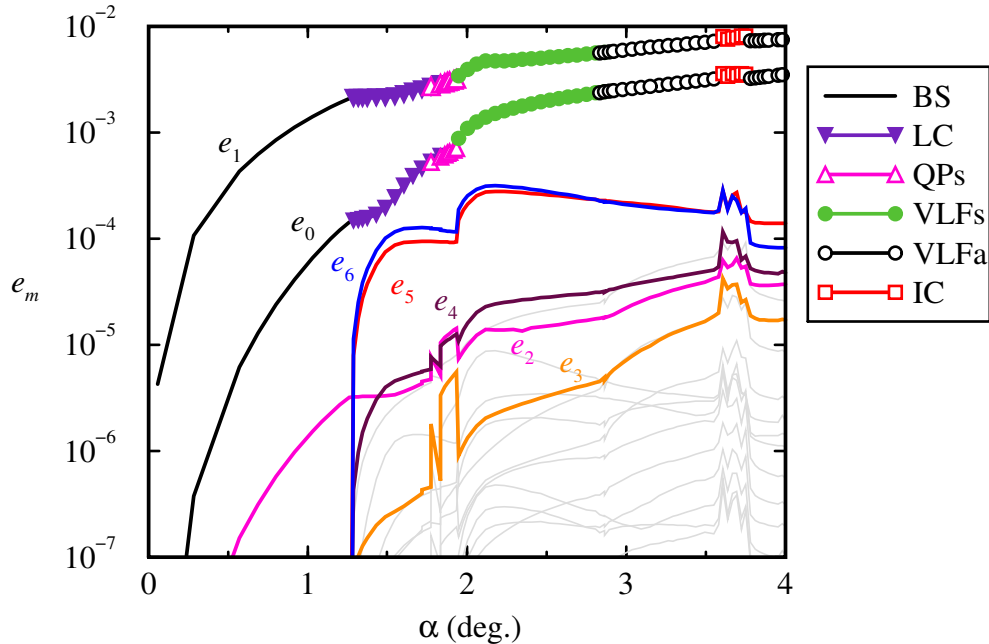


FIG. 4: Variation of e_m with α for the states dominated by the triadic-resonance-induced dynamics. Energies e_m with $m > 6$ are plotted in gray. The symbols correspond to the different states obtained in this α range, described in the text.

in Fig. 4. A good measure of the strength of the overturning flow is given by e_1 , and e_0 measures the $m = 0$ azimuthal mean flow departure from solid-body rotation and is a good proxy measure of the flow nonlinearity [16]. Figure 4 shows that the relevant components of the flow are the $m = 1, 5$ and 6 Fourier modes corresponding to the 1:5:6 triadic resonance, along with the $m = 0$ component. The remaining modal energies are at least one order of magnitude smaller than e_5 or e_6 , and therefore the dynamics are dominated by the triadic resonance mechanism. Approaching $\alpha = 4^\circ$, the remaining Fourier components start to grow, particularly the leading harmonics of the $m = 1$ overturning flow. As a result of nonlinear interactions, the triadic resonance modes $m = 5$ and 6 become increasingly modified, but are still clearly dominant over the harmonics of the forced $m = 1$ flow. We call this α -regime the weakly nonlinear resonant regime.

The complex flows, whose e_m are shown in Fig. 4, consist of states with either two or three incommensurate temporal frequencies, as well as a state which intermittently alternates between being quasiperiodic and temporally chaotic. Moreover, some of these states preserve \mathcal{I} -symmetry while others break it. Specifically, LC loses stability subcritically at $\alpha \approx 1.862^\circ$, and for slightly larger α the flow evolves to a quasiperiodic \mathcal{I} -symmetric state, QPs, which

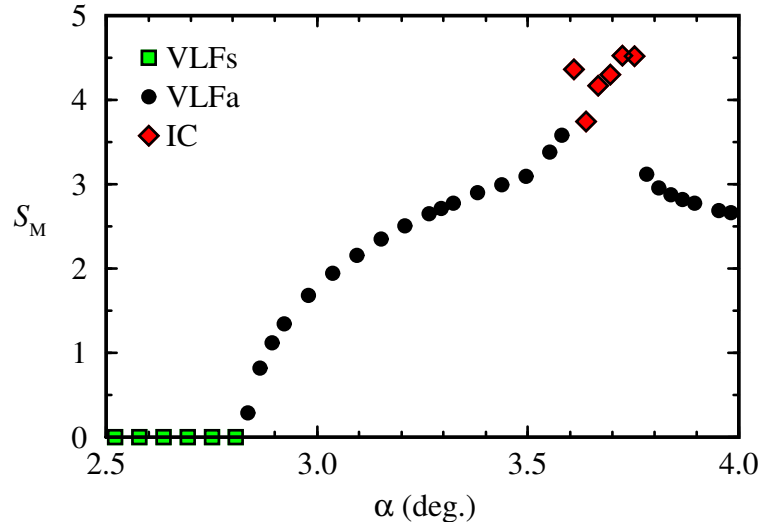


FIG. 5: Variation of the symmetry parameter S_M with α for the states dominated by the triadic-resonance-induced dynamics.

is basically a slow modulation of LC (see [16] for details). The QPs solution branch can be traced to lower α , and it loses stability at $\alpha \approx 1.748^\circ$, forming a hysteretic loop with LC for $\alpha \in (1.748^\circ, 1.862^\circ)$.

The QPs solutions lose stability for $\alpha \gtrsim 1.942^\circ$. The resulting flow is a very slow modulation of QPs, the new frequency being an order of magnitude smaller than the frequencies associated with QPs. This new very-low-frequency state, VLFs, is also \mathcal{I} -symmetry, and its spatio-temporal characteristics show it to be a slow drift in phase space between BS, LC and QPs (see [16] for details). VLFs undergoes a supercritical symmetry-breaking bifurcation at $\alpha \approx 2.82^\circ$, leading to VLFa. For α values near the bifurcation, the degree of symmetry breaking, as measured by S_M , is relatively small (see Fig. 5), and the overall spatio-temporal features of VLFa are very similar to those of VLFs. With increasing α , VLFa becomes more asymmetric, and when $S_M \approx 3.5$, the quasiperiodic VLFa becomes irregular, consisting of alternating episodes of chaotic and quasiperiodic temporal behavior. These intermittent chaotic states, IC, are found for $\alpha \in (3.610^\circ, 3.753^\circ)$, and for larger α the VLFa state is recovered and has S_M reducing slowly with increasing α , as shown in Fig. 5. These various states have also been obtained by fixing $\alpha = 1^\circ$ while increasing ω_0 , [16], but the order in which they appear with increased forcing is different.

The results discussed so far for increasing α are consistent with the single-point LDV measurements of [29], that reported a single peak at the forcing frequency (plus harmonics)

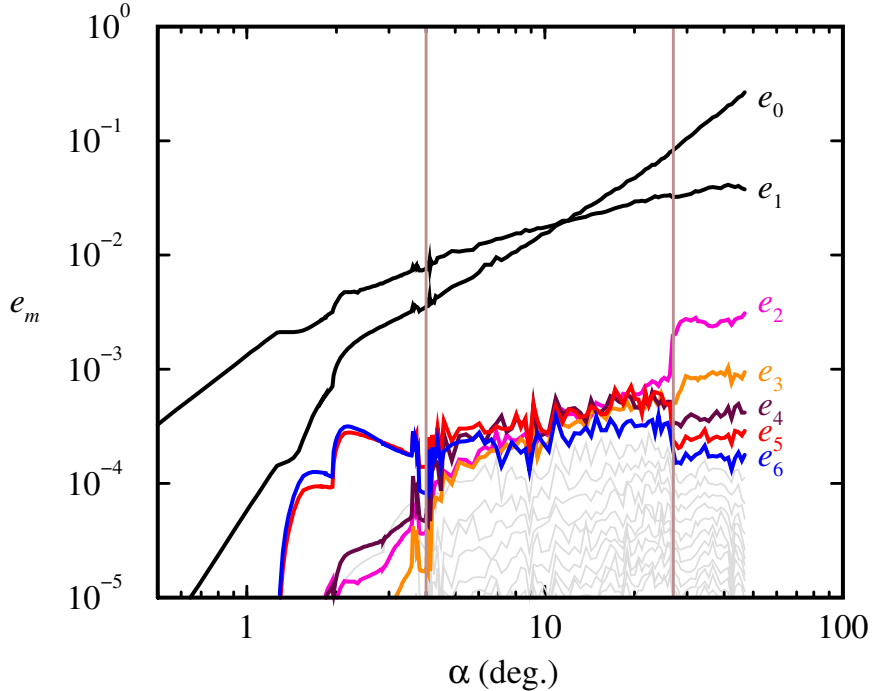


FIG. 6: Variations of e_m with α . The two vertical lines at $\alpha = 4^\circ$ and 27° demarcate three regimes of differing dynamics.

corresponding to the $m = 1$ Kelvin mode for $\alpha \in (1^\circ, 2.5^\circ)$, and for $\alpha \in (2.5^\circ, 3.5^\circ)$ the temporal spectra included a very-low-frequency component. For $\alpha \in (3.5^\circ, 5^\circ)$, a subharmonic component emerged (very likely related to the \mathcal{I} -symmetry-breaking process). Those experimentally observed temporal characteristics were reported to be consistent with the earlier flow visualizations of [8].

B. Strongly nonlinear resonant regime: $4^\circ \lesssim \alpha \lesssim 27^\circ$.

Increasing $\alpha \gtrsim 4^\circ$ results in an abrupt transition to a sustained temporally chaotic state, SC1, consistent with the observations of [8]. This abrupt transition between VLFa and SC1 has a small region of hysteresis, $\alpha \in (4.097^\circ, 4.125^\circ)$. Figure 6 shows the variations in energies e_m with the nutation angle over the range $\alpha \in [0.05^\circ, 47^\circ]$. The figure is plotted with a logarithmic scale for α in order to better view the details for small α . There are three clearly distinct regimes: for $\alpha \leq 4^\circ$, the dynamics were analyzed in the previous section and are dominated by the 1:5:6 triadic resonance. In the second regime, $\alpha \in (4^\circ, 27^\circ)$, the azimuthal Fourier components from $m = 2$ to 6 have comparable energies e_m , indicating

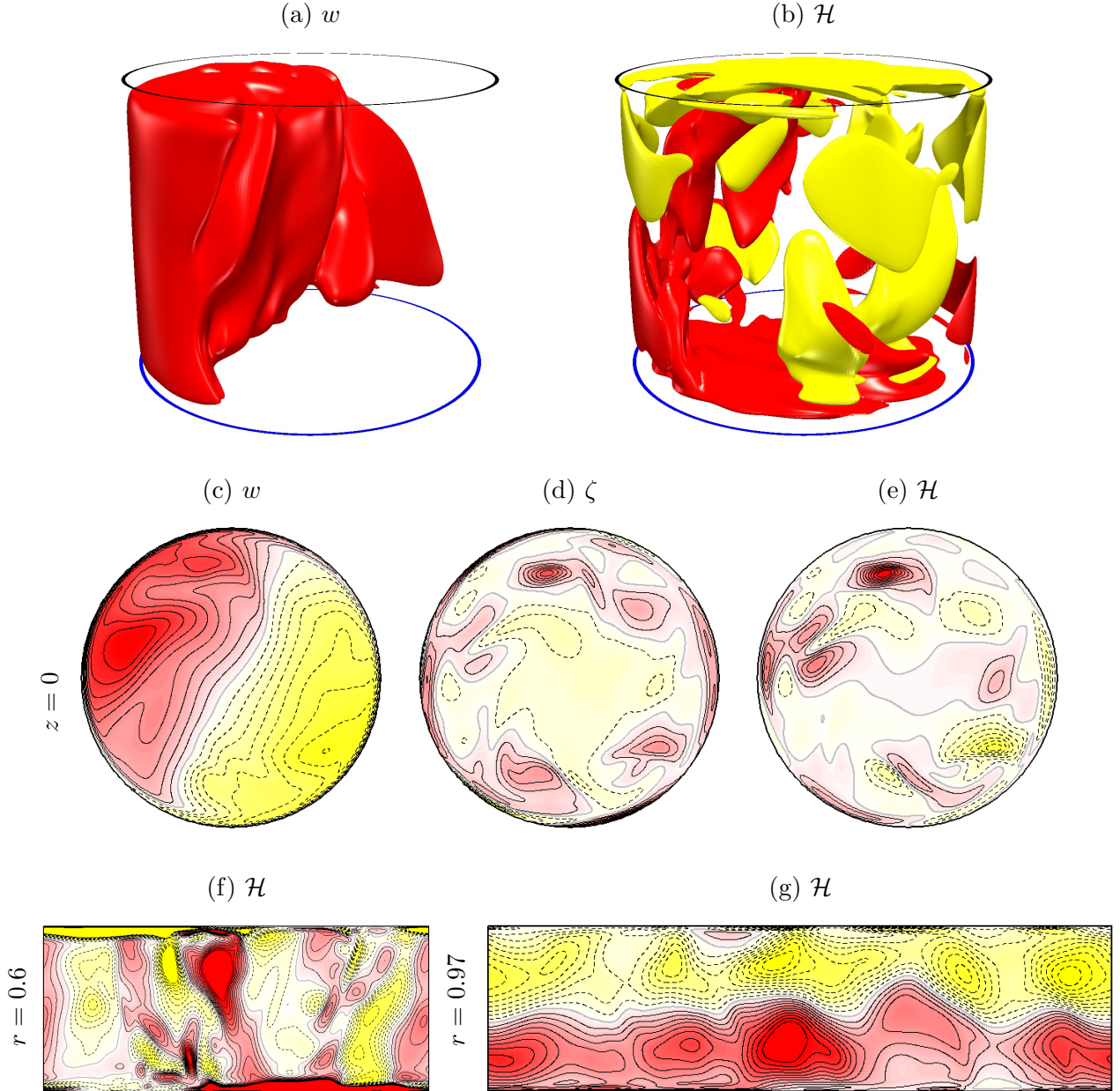


FIG. 7: SC1 at $\alpha = 8.6^\circ$: isosurfaces of (a) axial velocity and (b) helicity at levels $w = 100$ & $\mathcal{H} = \pm 2 \times 10^6$ (see the online movie [URL will be inserted by publisher]), and contours of (c) axial velocity, (d) axial vorticity, and (e) helicity, at mid-height $z = 0$; there are 20 contours equispaced between the minimum and maximum values in the section. Helicity contours in (θ, z) at (f) $r = 0.6$ and (g) $r = 0.97$; there are 20 contours equispaced between $\mathcal{H} \in [-4 \times 10^6, 4 \times 10^6]$.

that the 1:5:6 resonance is still at play, but that nonlinear interactions between these Fourier components and the $m = 0$ and 1 components are important. This regime is referred to as the strongly nonlinear resonant regime. In the third regime, $\alpha \geq 27^\circ$, the triadic resonance

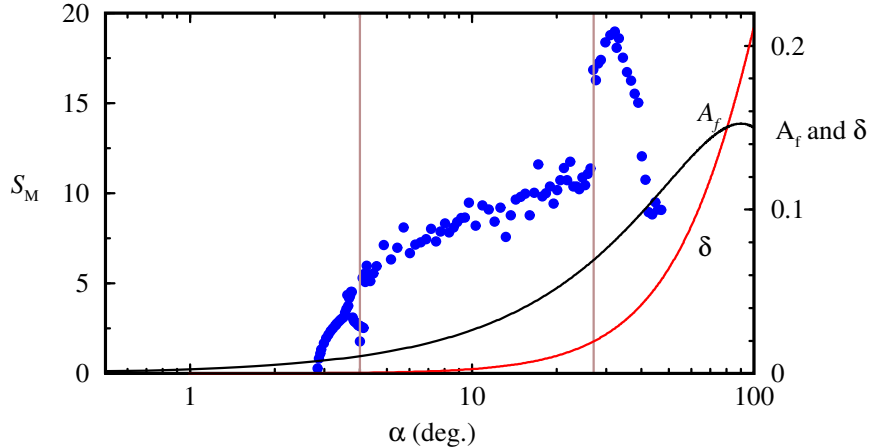


FIG. 8: Variations of S_M with α . The two vertical lines at $\alpha = 4^\circ$ and 27° demark three regimes of differing dynamics. Included are the variation of the amplitude of the forcing A_f and the detuning parameter δ with α (right vertical axis).

no longer plays any significant role, and will be described in the following section, §IV C.

Figure 7 shows a typical SC1 solution corresponding to $\alpha = 8.6^\circ$ (0.15 rad). The $m = 1$ overturning flow is twisted in the positive azimuthal direction with respect to the BS and LC laminar states, but remains mostly vertical (see Figs. 7a and 7c). The bulk flow still has helicity columns associated with the triadic resonance modes, clearly illustrated in the axial vorticity and helicity contours in the figure. However, these columns are no longer evenly distributed in azimuth. They span the whole height of the cylinder for a short time before breaking up into smaller pieces, followed by the formation of new columns, all in a spatio-temporally complex fashion (see the online movie associated with Fig. 7b). The structure of the sidewall boundary layer is still similar to the structure in the weakly nonlinear resonant regime, with positive helicity in the bottom half of the cylinder boundary layer and negative helicity in the top half, but the oscillations in the helicity at the mid-plane are more irregular.

C. Chaotic non-resonant regime: $\alpha \gtrsim 27^\circ$.

When $\alpha \gtrsim 27^\circ$, there is an abrupt change in the flow dynamics. Figure 6 shows that the energies of the Fourier components of the flow essentially become harmonics of the $m = 1$ overturning flow, which is now spatio-temporally complicated. Note in particular that the energies of $m = 5$ and 6, which for $\alpha \lesssim 27^\circ$ were dominated by the triadic-resonance-excited

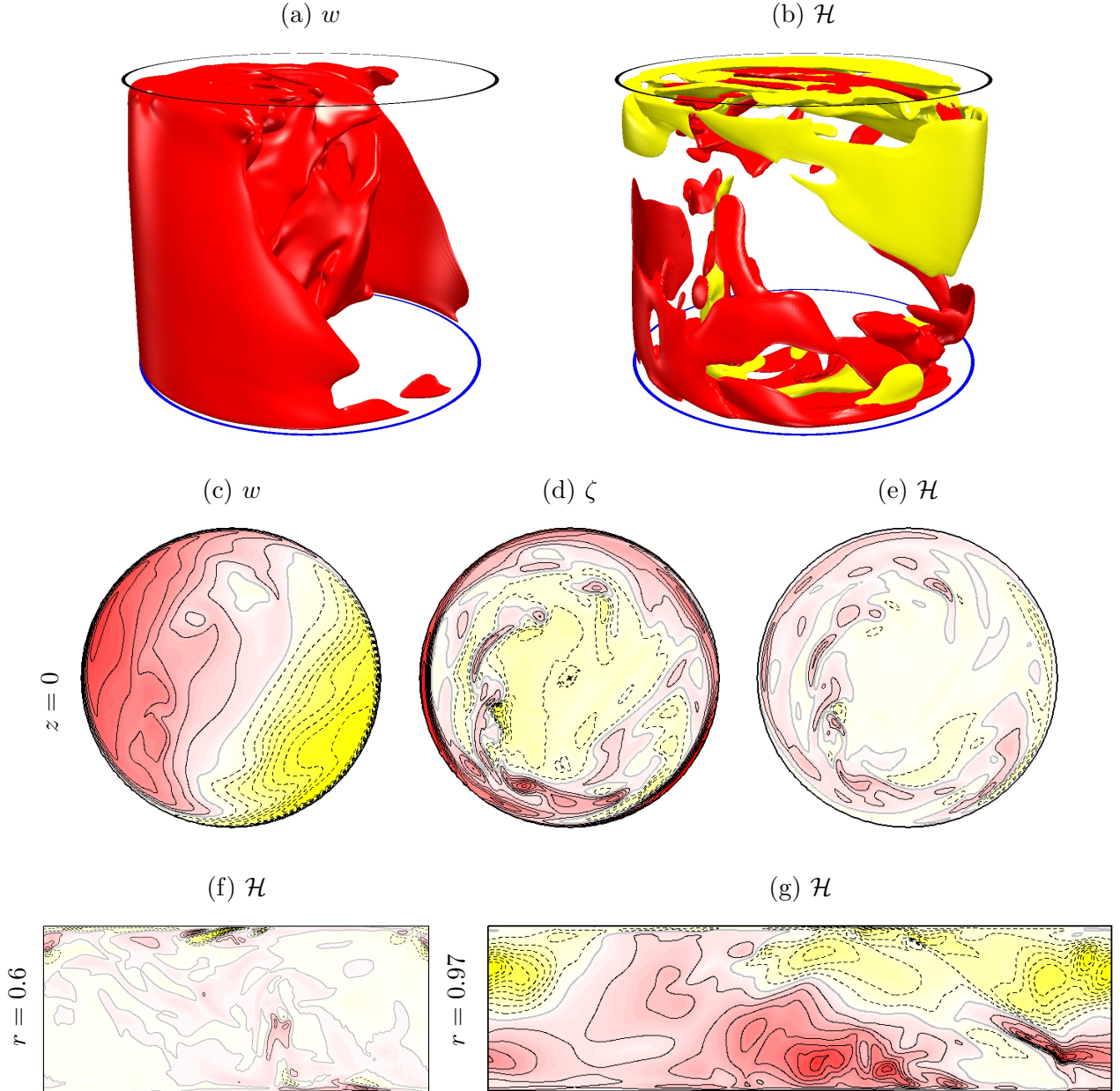


FIG. 9: SC2 at $\alpha = 32^\circ$: isosurfaces of (a) axial velocity and (b) helicity at levels $w = 100$ & $\mathcal{H} = \pm 1.2 \times 10^7$, and contours of (c) axial velocity, (d) axial vorticity, and (e) helicity, at mid-height $z = 0$; 20 contours equispaced between the minimum and maximum values in the section for w and ζ . Helicity contours in (θ, z) at (f) $r = 0.6$ and (g) $r = 0.97$. 20 contours equispaced between $\mathcal{H} \in [-6 \times 10^7, 6 \times 10^7]$ for (e), (f) and (g).

Kelvin modes $(1, 6, 2)$ and $(1, -5, 1)$, are now merely associated with the fifth and sixth harmonics of $m = 1$, and are significantly smaller. This abrupt change is also present in the degree of asymmetry of the flow, as quantified by S_M . Figure 8 shows how in the mid- α

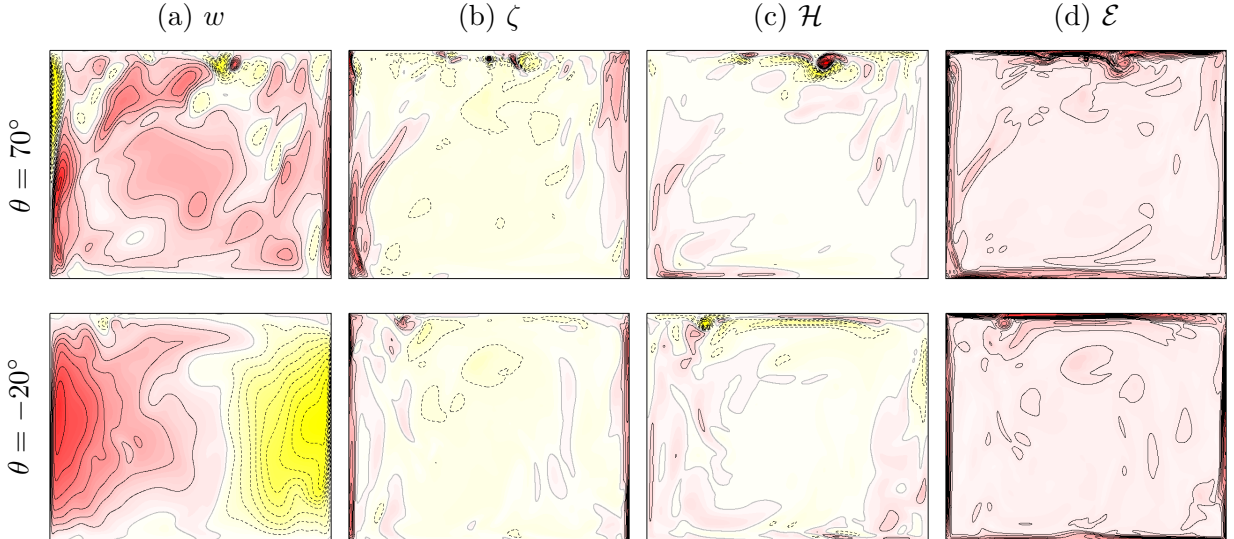


FIG. 10: SC2 at $\alpha = 32^\circ$ in orthogonal meridional planes; the plane $\theta = 70^\circ$ separates approximately the up and down parts of the overturning flow. There are 20 contours equispaced between the minimum and maximum values in the section for w , ζ and \mathcal{H} . For the enstrophy, there are 15 contours quadratically spaced in $\mathcal{E} \in (0, 8 \times 10^9)$.

regime, S_M for SC1 increases essentially monotonically with α , whereas in the high- α regime ($\alpha \gtrsim 27^\circ$), S_M makes a sudden jump, reaches a maximum at $\alpha \approx 32^\circ$ that is about twice as big as the largest S_M value for SC1, and then drops back to about the SC1 level. The flow in the high- α regime, SC2, is also spatio-temporally complicated, but of a very different nature compared to SC1.

Figure 9 shows various aspects of the SC2 state at $\alpha = 32^\circ$ (0.56 rad), where SC2 is most asymmetric. One change in SC2 compared to all the other states obtained in the two lower α regimes, is that the flow is strongly skewed. This is particularly evident in the sidewall boundary layer structure, where in the other states, the top half had negative helicity and the bottom half had positive helicity, while SC2 has an oblique plane separating the positive and negative \mathcal{H} boundary layer, oriented at roughly 45° . Another difference is that the interior flow is devoid of helical structures; the \mathcal{H} -columns that were associated with the triadic resonance modes and predominant in LC, QPs, VLFs, VLFA, and SC1, are completely absent. In SC2, the \mathcal{H} -structures in the interior are instead associated with shear layers separating from the side and endwall boundary layers. These are more readily

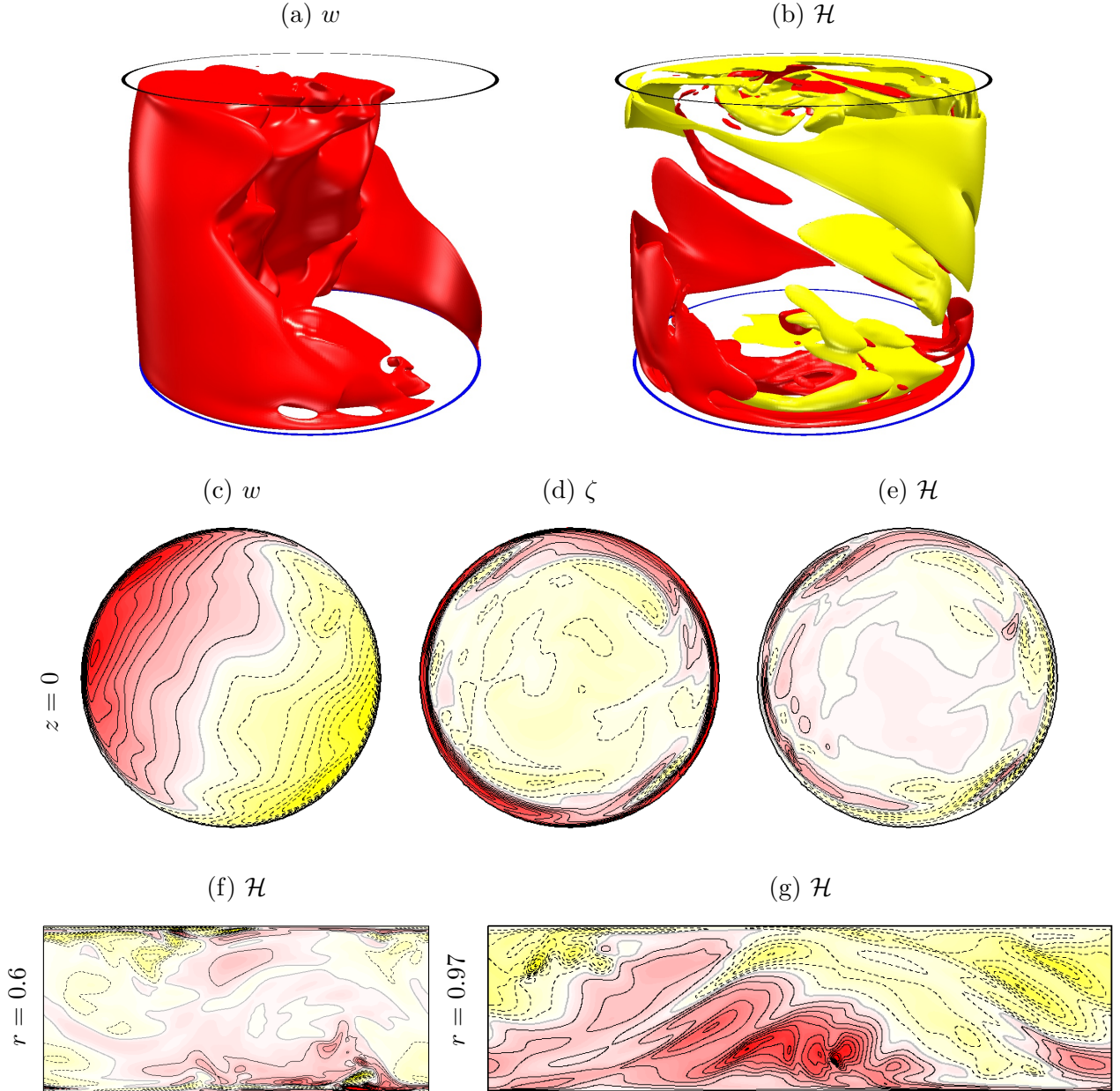


FIG. 11: SC2 at $\alpha = 47^\circ$: isosurfaces of (a) axial velocity and (b) helicity at levels $w = 100$ & $\mathcal{H} = \pm 2 \times 10^7$ (see the online movies [URL will be inserted by publisher]), and contours of (c) axial velocity, (d) axial vorticity, and (e) helicity, at mid-height $z = 0$; there are 20 contours equispaced between the minimum and maximum values in the section for w and ζ . Helicity contours in (θ, z) at (f) $r = 0.6$ and (g) $r = 0.97$; there are 20 contours equispaced between $\mathcal{H} \in [-6 \times 10^7, 6 \times 10^7]$ for (e), (f) and (g).

seen in the meridional plots shown in Fig. 10. The two meridional planes used in the figure correspond to the orientation of the overturning flow. The $\theta = 70^\circ$ plane roughly separates

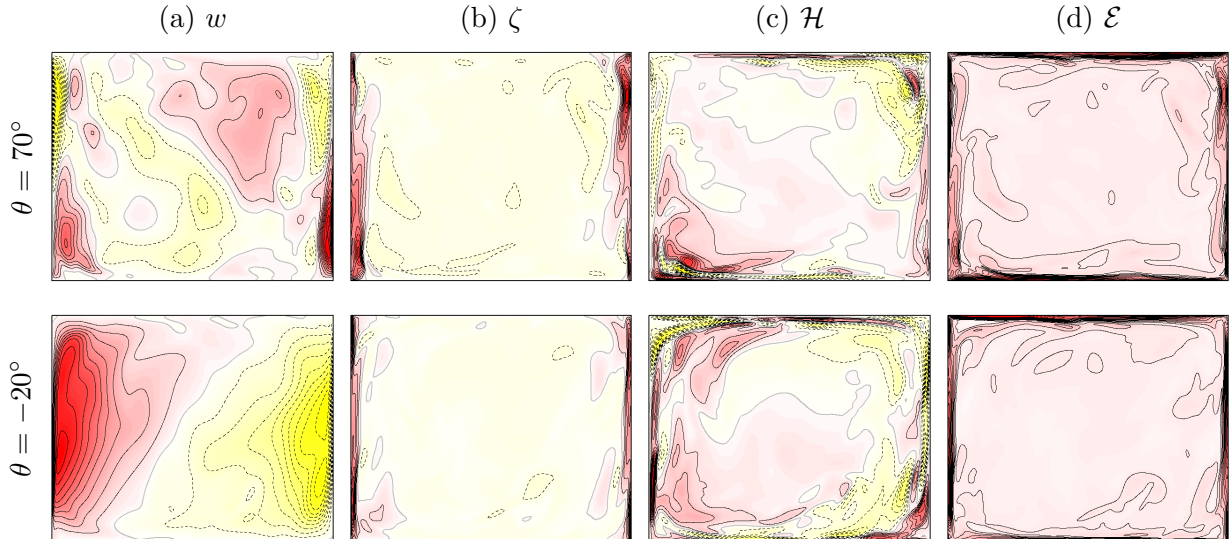


FIG. 12: SC2 at $\alpha = 47^\circ$ in orthogonal meridional planes; the plane $\theta = 70^\circ$ separates approximately the up and down parts of the overturning flow. There are 20 contours equispaced between the minimum and maximum values in the section for w , ζ and \mathcal{H} . For the enstrophy, there are 15 contours quadratically spaced in $\mathcal{E} \in (0, 8 \times 10^9)$.

the upward flow from the downward flow, and the $\theta = -20^\circ$ plane is orthogonal to the $\theta = 70^\circ$ plane. The variables plotted are w , ζ and \mathcal{H} , as in the earlier plots, along with the enstrophy, $\mathcal{E} = \frac{1}{2}|\nabla \times \mathbf{u}|^2$. All plots show, at this instant, strong separations at the top boundary layer, and a shear layer extending between the top and sidewall layers. The eruptions from the boundary layer observed in Fig. 10 (first row) are located at the top and left sidewall, and are almost absent at the bottom and right sidewall. This strong asymmetry results in a large value of S_M . Of course, the eruptions illustrated in Fig. 10 are an event at a given instant; these events change in an irregular way with time, appearing in different boundary layers erratically. There are no hints of the columnar structures associated with the $m = 5$ and 6 Kelvin modes.

The SC2 flow at the largest α considered in this study, $\alpha = 47^\circ$, is shown in Figs. 11 and 12. The overall flow structure has not changed. It is still predominantly an $m = 1$ overturning flow with a twisted sidewall boundary layer structure which has an oblique orientation, and the interior only has intermittent structures associated with boundary layer separations. However, there is a substantial decrease in the flow asymmetry as illustrated

in Fig. 8. This is due to the boundary layer eruptions being more prevalent than they were for $\alpha < 40^\circ$ and being more symmetrically distributed amongst the boundary layers. The overturning flow becomes oblique, following the oblique plane separating the positive and negative \mathcal{H} parts of the sidewall boundary layer (see Fig. 12a at $\theta = -20^\circ$), and the eruptions from the boundary layer take place mainly around the corners where the overturning flow is strongest (see Fig. 12c). The spatio-temporal structure of this state is illustrated in the online movie associated with Fig. 11(b).

V. DISCUSSION AND CONCLUSION

The main goal of the present study is the understanding of the influence of the nutation angle α on the precessing cylinder flow, and the sudden transitions to turbulence observed in experiments. Keeping $\Gamma = 1.62$, $\omega_0 = 4000$ and $\omega_p = -610$ fixed, and varying α from 0.5° to 47° , three different dynamic regimes have been identified from the Navier–Stokes simulations.

The main differences in these three regimes are illustrated in Fig. 8 in terms of the symmetry parameter S_M , that also includes the variation of the forcing amplitude A_f and the detuning parameter δ with α , and in Fig. 6 in terms of the energies of the relevant Fourier components of the flow. Note that e_0 and e_1 represent features that are present in all three regimes: the deviation from solid body rotation and the overturning flow, and we will focus on e_n for $n \geq 2$ in order to better emphasize the differences.

In the low- α regime ($\alpha \lesssim 4^\circ$), detuning effects are negligible, the precessional forcing is weak, and the dynamics are dominated by the triadic resonance. The $m = 5$ and 6 Fourier components of the flow have much larger energies than the other components with $m > 1$, as predicted by the weakly nonlinear theory [13]. However, additional bifurcations leading to quasiperiodic and weakly chaotic solutions occur for small increases in α . The inversion symmetry of the flow is broken at the bifurcation to VLFa, although the bifurcated solutions retain this \mathcal{I} -symmetry when averaged in time [16]. The boundary layers are very similar to the boundary layers of the steady base state solution, and the bulk of the flow is dominated by columnar vortices due to the triadic resonance mechanism.

In the mid- α regime ($4^\circ \lesssim \alpha \lesssim 27^\circ$), the detuning effects are still weak, the forcing is stronger, and the dynamics are spatio-temporally complex due to nonlinear interactions

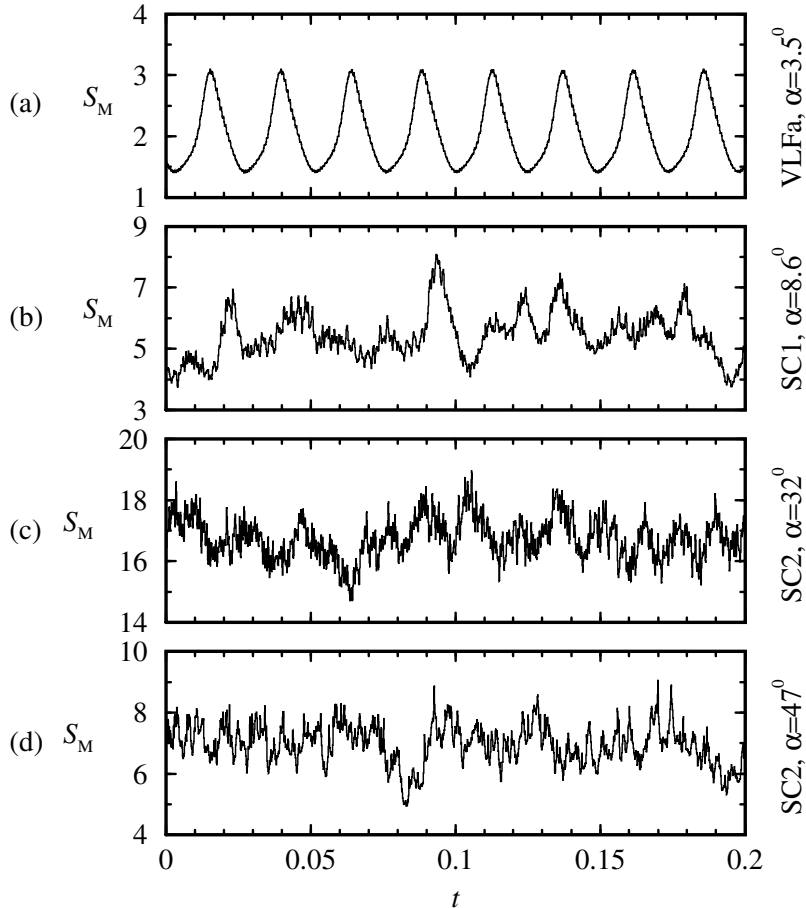


FIG. 13: Time series of S_M for the states indicated.

between the triadic resonance driven flow components and the nonlinear harmonics of the $m = 1$ overturning flow. As shown in Fig. 6, the energies e_i , $i \in [2, 6]$, have very similar levels. This is a clear indication of the strong interaction between the triadic resonance mechanism and the nonlinear effects. The symmetry parameter S_M increases steadily with α in this regime. The boundary layers are still similar to the boundary layers of the base state solution, but with larger deformations, and the columnar vortices in the bulk of the flow are still present, but they are no longer uniformly distributed in azimuth, and undergo break-up and reformation in a spatio-temporally complex fashion.

Figure 13 shows time series, over one fifth of a viscous time, of the symmetry parameter S_M for flows in each of the three α -regimes. Figure 13(a) corresponds to VLFa in the low- α regime at $\alpha = 3.5^\circ$. This state periodically approaches an unstable symmetric state (at the minima of S_M), moves away from it, and returns. The flow is periodic with three frequencies, the very-low frequency that is clearly apparent in the figure, a small modulation with much

larger frequency that is barely appreciable in the figure, and an azimuthal drift frequency which disappears in S_M because S_M is a global measure, and a rotation of the flow pattern does not modify S_M [16]. The other three states, in the mid- and high- α regimes, are clearly erratic in time, and we have called them sustained chaotic solutions, SC1 and SC2, respectively.

In the large- α regime ($\alpha \gtrsim 27^\circ$), the detuning is no longer negligible, and the amplitude of the forcing is larger than in lower- α regimes. Over a narrow interval in α , centered at $\alpha = 27^\circ$, the flow undergoes dramatic changes, as illustrated in Fig. 6. The energies of the Fourier modes $m = 2$ to 6, that were of comparable strength in the mid- α regime, change abruptly: all the energies e_m now decrease with increasing m , spread over more than a decade in energy levels. The Fourier components of the flow essentially become harmonics of the $m = 1$ overturning flow, and the triadic resonance mechanism does not play any significant role. There is also an abrupt increase in the flow asymmetry: S_M almost doubles and remains very high up to $\alpha \lesssim 40^\circ$. This is due to asymmetric eruptions from the boundary layers, that occur erratically with time and location in the various boundary layers. The sidewall boundary layer structure is also completely different to that in the lower- α regimes, with an oblique plane separating the positive and negative helicity parts of the boundary layer. The flow in the interior of the cylinder is devoid of helical columns, and the only structures that are apparent are related to the boundary layer eruptions forming short-lived internal shear layers that are predominantly located near the boundary layers. Increasing the nutation angle above 40° results in a decrease in the asymmetry of the flow. This is due to the boundary layer eruptions being more symmetrically distributed. The eruptions from the boundary layer take place mainly around the corners where the overturning flow is strongest. The interior of the cylinder does not exhibit any large scale structure.

The numerical simulations presented in this study show that the flow undergoes dramatic changes as the nutation angle α is increased while the remaining parameters are held fixed. The fixed parameters represent the geometry (Γ), the cylinder and table angular velocities and the fluid viscosity (ω_0 and ω_p). Of course, increasing α results in an increase in the amplitude of the forcing A_f (because the component of the rotation orthogonal to the cylinder axis (11) increases), and also produces a detuning away from the strict triadic resonance condition (12). There are various characteristics of the resulting flows that are directly associated with α : the distortion of the sidewall boundary layer, with an oblique

plane separating its positive and negative helical parts and the subsequent distortion of the overturning flow are clearly associated with the flow trying to accommodate to a total angular velocity that is widely misaligned with the cylinder axis for large α . In this high- α regime, e_0 is as much as 0.25, i.e. $E_0 \approx 0.25E_{SB}$. There is a massive disruption to the solid-body rotation associated with the cylinder rotation around its axis, on which the linear inviscid theory of Kelvin modes is based: the Kelvin eigenmodes from an infinitesimal perturbation to solid-body rotation around the cylinder axis. So, in this sense it is not surprising that Kelvin mode triadic resonance effects are not present in this high- α regime.

Acknowledgments

This work was supported by US NSF Grant CBET-1336410 and Spanish MECD Grant FIS2013-40880-P.

-
- [1] W. V. R. Malkus, *Precession of the Earth as the cause of geomagnetism*. Science **160**, 259 (1968).
 - [2] M. Le Bars, D. Cebbron, and P. Le Gal, *Flows driven by libration, precession, and tides*. Ann. Rev. Fluid Mech. **47**, 163 (2015).
 - [3] R. Manasseh, *Visualization of the flow in precessing tanks with internal baffles*. AIAA J. **31**, 312 (1993).
 - [4] G. Bao and M. Pascal, *Stability of a spinning liquid-filled spacecraft*. Arch. Appl. Mech. **67**, 407 (1997).
 - [5] S. A. Triana, D. S. Zimmerman, and D. P. Lathrop, *Precessional states in a laboratory model of the Earth's core*. J. Geophys. Res. **117**, B04103 (2012).
 - [6] S. Kida, *Steady flow in a rapidly rotating sphere with weak precession*. J. Fluid Mech. **680**, 150 (2011).
 - [7] S. Goto, A. Matsunaga, M. Fujiwara, M. Nishioka, S. Kida, and M. Yamato, *Turbulence driven by precession in spherical and slightly elongated spheroidal cavities*. Phys. Fluids **26**, 055107 (2014).
 - [8] R. Manasseh, *Breakdown regimes of inertia waves in a precessing cylinder*. J. Fluid Mech.

- 243**, 261 (1992).
- [9] A. D. McEwan, *Inertial oscillations in a rotating fluid cylinder*. J. Fluid Mech. **40**, 603 (1970).
- [10] R. Manasseh, *Distortions of inertia waves in a rotating fluid cylinder forced near its fundamental mode resonance*. J. Fluid Mech. **265**, 345 (1994).
- [11] R. Lagrange, C. Eloy, F. Nadal, and P. Meunier, *Instability of a fluid inside a precessing cylinder*. Phys. Fluids **20**, 081701 (2008).
- [12] P. Meunier, C. Eloy, R. Lagrange, and F. Nadal, *A rotating fluid cylinder subject to weak precession*. J. Fluid Mech. **599**, 405 (2008).
- [13] R. Lagrange, P. Meunier, F. Nadal, and C. Eloy, *Precessional instability of a fluid cylinder*. J. Fluid Mech. **666**, 104 (2011).
- [14] R. Lagrange, P. Meunier, and C. Eloy, *Triadic instability of a non-resonant precessing fluid cylinder*. C. R. Mecanique (2016). DOI:10.1016/j.crme.2015.12.002.
- [15] T. Albrecht, H. M. Blackburn, J. M. Lopez, R. Manasseh, and P. Meunier, *Triadic resonances in precessing rapidly rotating cylinder flows*. J. Fluid Mech. **778**, R1 (2015).
- [16] F. Marques and J. M. Lopez, *Precession of a rapidly rotating cylinder flow: traverse through resonance*. J. Fluid Mech. **782**, 63 (2015).
- [17] Y. Lin, J. Noir, and A. Jackson, *Experimental study of fluid flows in a precessing cylindrical annulus*. Phys. Fluids **26**, 046604 (2014).
- [18] R. R. Kerswell, *Elliptical instability*. Ann. Rev. Fluid Mech. **34**, 83 (2002).
- [19] I. Mercader, O. Batiste, and A. Alonso, *An efficient spectral code for incompressible flows in cylindrical geometries*. Computers and Fluids **39**, 215 (2010).
- [20] J. M. Lopez and F. Marques, *Sidewall boundary layer instabilities in a rapidly rotating cylinder driven by a differentially co-rotating lid*. Phys. Fluids **22**, 114109 (2010).
- [21] J. M. Lopez and F. Marques, *Instabilities and inertial waves generated in a librating cylinder*. J. Fluid Mech. **687**, 171 (2011).
- [22] J. M. Lopez and F. Marques, *Instability of plumes driven by localized heating*. J. Fluid Mech. **736**, 616 (2013).
- [23] J. M. Lopez and F. Marques, *Rapidly rotating cylinder flow with an oscillating sidewall*. Phys. Rev. E **89**, 013019 (2014).
- [24] G. B. Arfken and H. J. Weber, *Mathematical Methods for Physicists*. Academic Press, 6th edition (2005).

- [25] H. P. Greenspan, *The Theory of Rotating Fluids*. Cambridge University Press (1968).
- [26] X. Liao and K. Zhang, *On flow in weakly precessing cylinders: the general asymptotic solution*. J. Fluid Mech. **709**, 610 (2012).
- [27] D. Kong, Z. Cui, X. Liao, and K. Zhang, *On the transition from the laminar to disordered flow in a precessing spherical-like cylinder*. Geophys. Astrophys. Fluid Dyn. **109**, 62 (2015).
- [28] J. Jiang, D. Kong, R. Zhu, and K. Zhang, *Precessing cylinders at the second and third resonance: Turbulence controlled by geostrophic flow*. Phys. Rev. E **92**, 033007 (2015).
- [29] J. J. Koblence, *Inertial wave dynamics in a rotating and precessing cylinder*. J. Fluid Mech. **303**, 233 (1995).